ADVANCED FUNCTIONAL MATERIALS
www.afm-journal.de

Scintillator of Polycrystalline Perovskites for High-Sensitivity Detection of Charged-Particle Radiations

Mátyás Hunyadi, Gergely Ferenc Samu, Lóránt Csige, Attila Csík, Csaba Buga, and Csaba Janáky**

Herein, the first study on the scintillation properties of $CsCu_2X_3$ and $Cs_3Cu_2X_5$ (where X: Cl^-, Br^-, I^-) is presented, describing their charged particle-induced luminescence involving electrons, protons, α-particles, and heavy ions, as well as revealing their capabilities on the timing and spectroscopic evaluation of single-particle events. The thin layers are prepared with a simple and cost-effective deposition procedure, without the incorporation of external dopants, exploiting the intrinsic radiative recombination observed in low-dimensional perovskites. The combined effect of the high binding energy and localized stability of self-trapped excitons, large Stokes shift, defect tolerance, and the high excitation density along the particle track leads to the emergence of boosted scintillation pulses. The observations demonstrate the first use of inorganic thin-film scintillators with optical pulse characteristics and light yield competitive with doped single crystal scintillators, while also providing improved structural and functional stability under extreme environmental conditions.

1. Introduction

Scintillating materials are vital components of detector systems for non-destructive imaging applications in homeland security, medical diagnostics, high-energy physics, space exploration, or nuclear industry.[1] The role of scintillators is to efficiently absorb and convert high-energy radiation into detectable photons acquiring information on its energy, type, and moment of incidence. While the most widely used single-crystal scintillator materials (e.g., NaI:Tl, LYSO:Ce, $LaBr_3$:Ce, $CdWO_4$) have intensively been developed for decades, materials engineering aims to develop efficient scintillators with improved performance responding to novel challenges of their application, to the need for simplified and versatile fabrication, or to introduce new additional properties such as flexibility. In this vein, research areas emerged, extending traditional solutions of activator doping such as i) exploring new material compositions, various hybrids and metamaterials,[1] ii) nanostructuring of existing materials, or iii) producing thin films. The disruptive emergence of metal-halide perovskites as X-ray and γ-ray scintillators[2–5] also invigorated the search for new efficient materials for scintillator applications, gradually focusing on lead-free alternatives.

In most applications, bulk single crystals of scintillators are favored to ensure the effective absorption of γ-rays, X-rays or high-energy particles, when detailed spectroscopic information are needed. Thin-layer scintillators are generally considered for a few specific tasks, almost exclusively involving phosphor screens for X-ray imaging.[6] The few selected exceptions comprise the detection of high-fluence ionic beams employed in plasma diagnostics (e.g., in tokamak)[7] or fission-fragment counters.[8] In most nuclear and high-energy physics experiments, as well as in radiation monitoring, the spectroscopic detection of single-event incidences can also be of fundamental importance, matching the requirements of experiments focusing on the measurement precision of energy, timing, and optionally the radiation tracking. In practice, detectors engineered specifically for charged-particle detection cannot improve the precision of these quantities in parallel. This challenge is often solved by building hybrid detector systems, involving semiconductor-based charge calorimeters for spectroscopy, scintillators for timing detection, and ionization chambers for particle tracking. At the same time, the higher technical complexity of such experiments infers further operational difficulties and requires subtle reduction procedures of huge data sets. So far, great efforts have been devoted to the development of scintillators at least to partially unify the capabilities of simultaneously recording energy and timing information with a satisfactory precision by finding the optimum between the two extremes of scintillation behavior, represented with fast (plastics) and high luminosity (inorganic single

M. Hunyadi, L. Csige, A. Csík, C. Buga
Institute for Nuclear Research
Bem tér 18/c, H-4026 Debrecen, Hungary
E-mail: hunyadi.matyas@atomki.hu
G. F. Samu, C. Janáky
Department of Physical Chemistry and Materials Science
Interdisciplinary Excellence Centre
University of Szeged
Aradi Square 1, H-6720 Szeged, Hungary
E-mail: janaky@chem.u-szeged.hu
The ORCID identification number(s) for the author(s) of this article can be found under https://doi.org/10.1002/adfm.202206645.

DOI: 10.1002/adfm.202206645

crystalline) materials.[9] A critical property of heavy-element containing scintillator crystals is their volumetric sensitivity to γ-rays that can be reduced by decreasing the thickness of the scintillator layer to adopt to the stopping range of particles to be analyzed. The involvement of thin layers in scintillation detectors can be decisive in practical situations when an excessive yield of background radiation impedes the observation of rare nuclear processes or trace-level radioactivity.

The fabrication of thin layers or films raises a variety of technological obstacles or structural instabilities in most scintillator materials.[6] In a limited number of experiments plastic thin-film scintillators were already tested for particle detection (e.g., in the special case of heavy-ion radiations by replacing avalanche gas detectors).[8] The low light yield and consequently the poor energy resolution, however, considerably limit their more general use in nuclear applications. Similarly, the fabrication of thin film scintillators from highly luminescent inorganic single-crystals is also unconventional, where other drawbacks arise rooting in their high fabrication costs, and unfavorable physico-chemical properties such as the increased probability for fracturing,[10] or hygroscopicity.[11] In recent years, alternative materials emerged based on micro- and nanostructured,[12] polycrystalline,[13] powder-based or ceramic compositions of both conventional[14] and low-dimensional (0D, 1D) perovskites,[15] mostly with the aim of developing high-performance X-ray screens. In spite of the growing popularity of novel types of thin film scintillators, single-event detection has not been demonstrated for charged particles.

All-inorganic ternary copper halides (TCHs) are newcomers to the field of radiation detection.[16,17] Among these, the most frequently studied variants are $CsCu_2X_3$ and $Cs_3Cu_2X_5$ (where X: Cl^-, Br^-, I^-). Through compositional engineering, their optoelectronic properties – characterized by the photoluminescence (PL) peak position, width, and PL lifetime – can be fine-tuned.[18,19] TCHs are less toxic, photostable, more moisture, and heat resistant[20] compared to conventional lead halide perovskites.[21] TCHs attracted significant attention because of their near unity PL quantum yield and large Stokes shift, which makes them viable candidates for efficient light-emitting materials.[22] These properties are related to the 0D-arrangement of the octahedral compartments, which results in the quantum confinement of charge carriers, while in combination with the sufficiently strong exciton–phonon coupling (i.e., large exciton binding energies) fosters radiative recombination through self-trapped-excitonic (STE) states.[18] The intrinsic nature of the trapping and recombination processes on STE states circumvents saturation effects, and the breakdown of energy proportionality, which is often observed at color centers in doped scintillators at high excitation densities. This is critically important when the scintillator is exposed to MeV-range ion beams, reaching a maximum excitation density in the Bragg region of the particle track.[23] This behavior is considered a general phenomenon in low-dimensional perovskites and the underlying reason for the observed high quantum yields.[18]

TCHs can efficiently detect X-rays and γ-rays with excellent light yield, good energy resolution, and minimal afterglow.[22,24–27] These materials exhibit remarkable stability and radiation hardness, as operation was demonstrated for $CsCu_2I_3$-based devices during high-dose exposure of X-rays,[21] as well as by our stability tests presented below. Apart from their inherent radioluminescence, coupled with UV emitting scintillators (e.g., CsI:Na), further efficiency increase can be realized through down-conversion of the UV light.[28] Furthermore, through mixing complementary emitting variants, broadband white-light emissive scintillation layers can also be realized.[29,30] In these X-ray and γ-ray detection applications single-crystals[24,27,31,32] and thin films exhibited similar performance. Currently the most widespread thin film preparation strategies are i) the drop casting of TCH nanoparticle dispersions,[22,26] mixing of pre-synthetized powders with appropriate binding agents,[25,33,34] or the vacuum evaporation of the TCH compounds.[21]

In this paper, we report the preparation of $CsCu_2I_3$ and $Cs_3Cu_2I_5$ films with controllable thickness by a simple spray-coating procedure. To the best of our knowledge this is the first experimental study on inorganic polycrystalline thin-film scintillators that exhibit radioluminescence (RL) yield comparable to that of most commercial scintillators in the detection of a wide range of charged-particle types from electrons and light nuclei to fission-fragments.

2. Results and Discussion

The desired stoichiometric amounts of the CsI and CuI precursors were dissolved in an acetonitrile/water mixture and used as the spray-coating solutions, to prepare the $Cs_3Cu_2I_5$ or $CsCu_2I_3$ films with tunable thickness (up to 100 µm, Figure S1, Supporting Information) on different substrates (including flexible plastic sheets, Figure S2, Supporting Information). XRD measurements of the layers revealed the formation of the desired compounds with phase-pure composition, in their polycrystalline form (**Figure** 1; Figure S3a, Supporting Information). Details about the surface roughness, composition, and morphology of the films are shown in the Supporting Information (Figures S5–S9, Supporting Information).

The optical properties of the films were probed by UV–vis and steady-state PL spectroscopy (Figure 1b; Figures S3b and S4a, Supporting Information). From the UV–vis spectra bandgap values of 3.70 eV for $Cs_3Cu_2I_5$ and 3.74 eV for $CsCu_2I_3$ were determined. After excitation with 300 nm monochromatic light, both materials exhibit a broad PL signal, which is notably shifted compared to their respective absorption edge, characteristic of self-trapped excitons, caused by photo-induced lattice distortions due to the significant electron-phonon coupling.[22] This results in blue ($\lambda \approx 440$ nm) and yellow-green ($\lambda \approx 570$ nm) luminescence in $Cs_3Cu_2I_5$ and $CsCu_2I_3$ films, respectively. The determined absolute quantum yield (Figure S4, Supporting Information) was 71 ± 5% for the $Cs_3Cu_2I_5$ and 4.1 ± 0.4% for the $CsCu_2I_3$ layers. These values are in agreement with the values reported in the literature (see summary in Table S1, Supporting Information). At the respective PL peak positions, we monitored the decay of the PL signal (Figure 1c; Figure S3c, Supporting Information). In the case of $Cs_3Cu_2I_5$ the decay profile is fitted with a single exponential function, which can be attributed to single-species STE recombination.[35] The fit included a constant pedestal attributed to a weak long-term afterglow. Conversely, in $CsCu_2I_3$ layers a biexponential decay

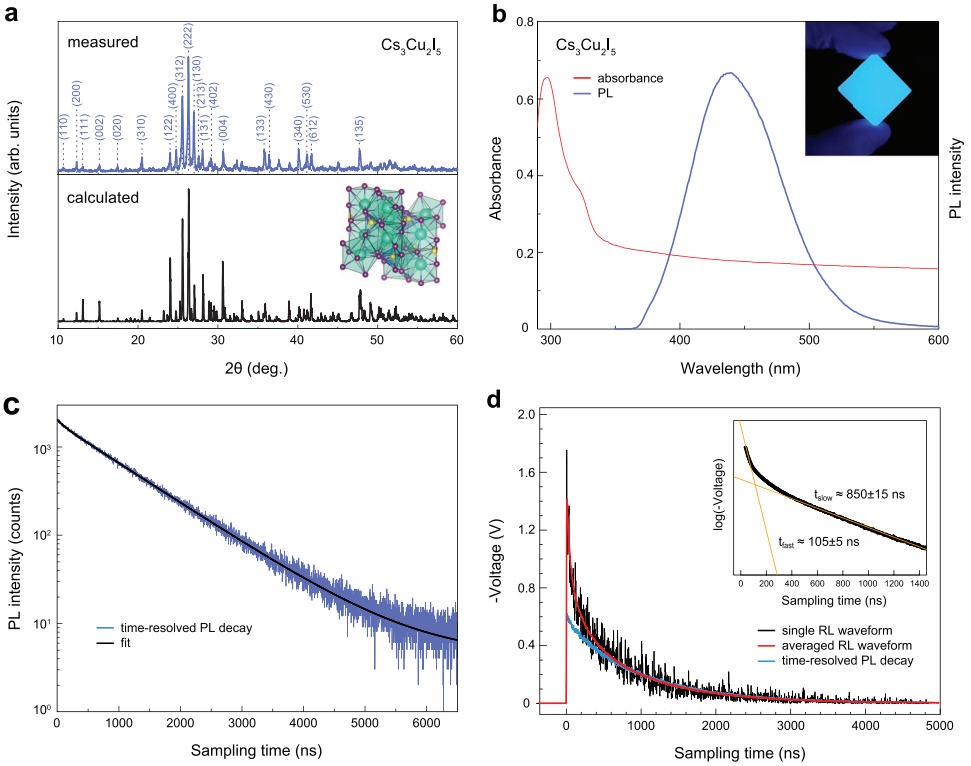

Figure 1. a) XRD pattern of the spray coated $Cs_3Cu_2I_5$ film, together with the simulated diffraction pattern, and simulated crystal structure. b) Steady-state PL measurement and UV–vis absorption spectra of a $Cs_3Cu_2I_5$ film. The insert shows a photograph of a $Cs_3Cu_2I_5$ layer on glass illuminated with UV light (385 nm). c) PL decay measurements of the same films measured at 440 nm. The excitation wavelength was 300 nm in all cases. d) Waveforms of RL response induced by α-particles (5.5 MeV). The PL decay of the same film is also plotted for comparison. The insert shows the biexponential fit of the averaged waveform with statistical parameters determined for five samples.

was observed that might be related to the presence of multiple excitonic species or the prevalence of surface trap states competing with STE recombination.[36]

The RL response of TCH thin layers following the exposure to single-particle radiation is fully characterized with the electric pulse waveform recorded with a waveform digitizer as shown in Figure 1d. The analysis of the α-RL waveforms revealed a composite decay pattern described with a biexponential model, decomposed to fast and slow components. The origin of this decay profile can be explained by the excitation density-dependent STE recombination and emerging higher-order terms of exciton-exciton interactions.[37] Time-resolved PL measurements resulted in a satisfactory agreement with the slow decay component of the particle-RL waveform, but the fast component was not apparent (Figure 1d). This might be rooted in the moderate excitation power of the laser beam that cannot reach the magnitude of STE densities typically generated when exposed to particle radiation.[38] A summary of all these optoelectronic parameters, compared with literature values are given in Table S2 (Supporting Information).

The fundamental parameters of scintillators quantifying their optical response are the luminous efficiency and decay time constants. For the specific case of α-RL response, literature data are scarcely available, nevertheless we have performed an extensive survey on the most widely used commercial scintillators for the comparison with the two copper-iodide compositions of this study (**Figure 2**a). TCH scintillators are located in the mid-range of the distribution fitting the general trends, while being the only polycrystalline materials. Importantly, the applicability of some materials in particle detection is hindered because of internal radioactivity,[39] especially at low radiation currents, or because of their susceptibility to radiation damage and thermal shock effects.[10] As displayed in Figure 2b, we categorized the scintillators listed in Figure 2a according to various hindrance factors, which emphasized the exceptional nature of TCH films by not sharing the disadvantages of the majority of these materials.

The statistical distributions of RL yields were determined in terms of photon counts per deposited energy and compared for the TCH family with measurable luminosity (Figure 2c). Apparently, the iodide containing variants produce α-RL light yields comparable to that of commercial scintillators resulting in 7500 ± 600 photon MeV^{-1} and 1700 ± 200 photon MeV^{-1} for $Cs_3Cu_2I_5$ and $CsCu_2I_3$, respectively, while other compositions are too faint for their feasible application as scintillators. The light yields and average lifetimes of the α-RL waveforms are evaluated with nonlinear regression methods and listed in Table S2 (Supporting Information). Importantly, the RL response of TCH thin layers has also been evaluated on a wider scope of charged particle radiations from electrons to heavy ions by considering the expectations that radiation measurements must be capable of separating different radiation components. This is important, because signals of background events (such as elastic scattering or secondary particles) can often

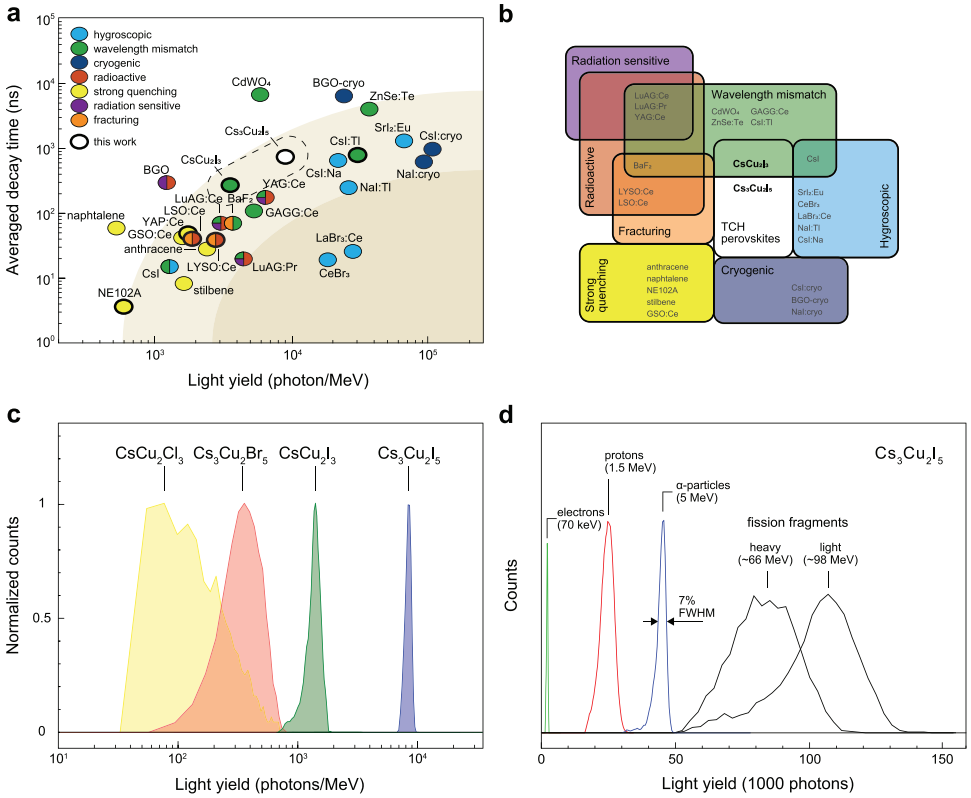

Figure 2. a) Correlation plot of light yield and decay time parameters of widely used scintillators for comparison with thin layers of $CsCu_2I_3$ and $Cs_3Cu_2I_5$. The scintillators are categorized by technical and physicochemical parameters that restrain their use for particle detection as thin-film scintillators; b) Principal grouping plot of scintillator materials listed in panel (a); c) Comparison of light yield distributions measured for different TCH compositions and d) charged-particle radiations tested with the TCH layers.

overlap and statistically suppress the observation of reaction channels in question (Figure 2d). The proton-RL light yield was 16 600 ± 400 photon MeV^{-1}.

The RL response of scintillators induced by nucleonic particles is lower than the X-ray or electron induced yields, due to the collisional recoil quenching: heavier ionic species transfer a larger fraction of their kinetic energy to lattice vibrations.[40] Therefore, the knowledge of electron-RL yield measured with a Compton-coincidence setup (CCT)[41] (Figure S11b, Supporting Information) is essential to evaluate the TCH compositions with respect to conventional scintillators, as well as helps to understand the excitation and recombination processes. The electron-RL yield was measured 22.3 ± 1.5 photons keV^{-1} (Figure S12a,b, Supporting Information), which is taken to calculate the α/β and proton/β quenching factors for $Cs_3Cu_2I_5$, giving 0.34 ± 0.04 and 0.74 ± 0.06, respectively. These values fit to general trends of scintillators, however, data on ion radiations other than α-particles are scarcely available in the literature.[40]

The RL response of TCH layers was evaluated in comparison with well-studied scintillator materials representing excellent timing (e.g., plastic, LYSO:Ce) and spectroscopic (e.g., CsI:Tl) performance. As demonstrated on the examples of $Cs_3Cu_2I_5$ and $CsCu_2I_3$, the leading edge of the pulse waveforms are plotted together with those of a slow (CsI:Tl) and fast (LYSO:Ce) inorganic, as well as a fast plastic (NE102A) scintillator in **Figure 3**a. The waveforms are synchronized by software at a level slightly above the electronic noise, cancelling out the contribution of transit time spread of the photomultipliers (PMTs). Therefore, the observed broadening determined at an arbitrarily set threshold (here 10 photons MeV^{-1} ns^{-1}) can be attributed to the interplay of stochastic processes of energy deposition, excitation transfer, and photon statistics. Doped scintillators exhibit significantly larger broadening, which is supposed to be the consequence of excitation transfer and their sequential trapping at emission centers being introduced as an additional uncertainty factor. Similarly, the α-RL yield and corresponding resolving power of particle energy measurement are also compared for commercial scintillators and the $Cs_3Cu_2I_5$ film presenting a transition of spectroscopic functionality between the extremes of high luminosity and fast RL response materials (Figure 3b,c). The energy resolution of the $Cs_3Cu_2I_5$ film was determined with the single α line of ^{241}Am yielding a peak width of 7% FWHM (Figure 2d), which made the partial separation of α lines visible emitted from a calibration source of various radioisotopes at distances of ≈320 keV (Figure 3b). On a broader scale of α-particle energy, the proportionality of the RL response was tested with a linear model for $Cs_3Cu_2I_5$ and $CsCu_2I_3$ films (Figure S13, Supporting Information).

A principal argument in favor of the use of thin-film scintillators versus bulk single crystals is their inherent insensitivity to γ-rays, which can be detrimental for monitoring very low radiation intensities. A comparative measurement was carried out irradiating a bulk (6 × 4 × 20 mm^3) LYSO:Ce crystal and a 50 µm thick $Cs_3Cu_2I_5$ film with α (^{241}Am) and γ-sources (^{60}Co)

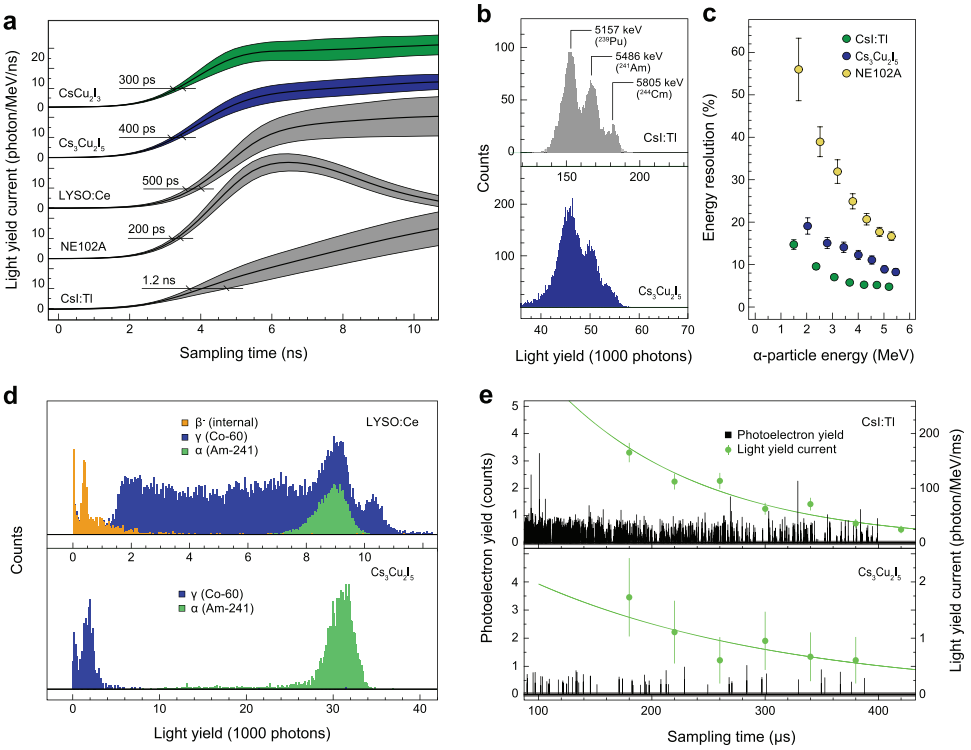

Figure 3. a) Rising edge of waveforms recorded for selected commercial scintillators in comparison with $Cs_3Cu_2I_5$ and $CsCu_2I_3$ thin layers. The ribbon plot represents the rms deviation of waveforms with respect to their mean synchronized with software triggering above the noise level. b) Light yields of α-RL compared for CsI:Tl bulk and $Cs_3Cu_2I_5$ thin layer scintillators for demonstrating the resolving power. The α-particles were emitted by a mixed source with components of nearly equidistant energy spacing. c) Energy resolution as FWHM peak width of α-RL spectra for scintillators shown in panel (b). d) Light yield spectra compared for LYSO:Ce bulk and $Cs_3Cu_2I_5$ thin-layer scintillators simultaneously irradiated with γ-ray and α-particles. e) Afterglow intensities demonstrated by summing 30 single α-RL waveforms for CsI:Tl and $Cs_3Cu_2I_5$ thin layer. Light yield currents were also derived by moving integration of averaged waveforms (green points) and fitted with an exponential decay model.

using the same irradiation geometry. Since the Compton background is always present in bulk scintillators with dimensions below their radiation length, rare α-incidences cannot be confidently identified, while thin film scintillators are considered more efficient in separating such accompanying radiation components (Figure 3d).

The practical value of scintillators is also affected by the level of afterglow intensity, mostly on the millisecond timescale. This can greatly affect the performance of imaging techniques relying on the fidelity of transmission of radiation intensity in CT or PET scanners, and can also be relevant for the spectroscopic detection of high-intensity particle radiations. The afterglow is a typical weakness of halide scintillators, prominently observed in CsI:Tl. In Figure 3e the comparison of CsI:Tl and $Cs_3Cu_2I_5$ scintillators reveals a considerable difference between their afterglow intensities in the sub-ms range indicating the suppressed effect of recombination in surface trap states of grain boundaries despite of their high concentration in polycrystalline $Cs_3Cu_2I_5$.

From a practical point of view, the use of scintillators for heavy-ion detection has always been desired by its simplicity, however, it is still considered an unconventional solution due to the strong recoil effect that is responsible for the observed low RL yields. To probe the heavy-ion RL response of TCH thin-films we installed a pair of $Cs_3Cu_2I_5$/PMT detectors in an experimental arrangement commissioned for studying nuclear fission processes in actinides (**Figure 4**a). Fission fragments (ff) are emitted at nearly opposite directions from the prefission nuclei here, excited with a 12 MeV proton beam bombarding an enriched ^{235}U target. The mass and velocity distributions of fission fragments are typically asymmetric at low excitation energies, the latter peaking at 1 and 1.4 cm ns^{-1} for the heavy and light fission fragment components, respectively. The time-of-flight (TOF) difference measured between the moments of arrival to the detectors is used to deduce the mass distribution, which in correlation with the ff-RL yield outlines the well-known double-humped structure apparently separating the two fragment groups (Figure 4a). As seen in Figure 4b, the distribution can also be projected along the axis of ff-RL yield, which is smeared out by the strong quenching effect with its subtle dependence on fragment mass and kinetic energy. The TOF-difference distribution was also calculated with the GEF model code,[42] which gave a satisfactory fit on the measured data assuming that (p,ff), (p,p'ff), and (pn,ff) reaction channels all contribute to the net fission yield (Figure 4c). In general, a severe restriction of fission studies is the presence of an overwhelming rate of γ-rays even from prompt emission or from the deexcitation of in-flight fission fragments. To detect fission fragments, low-pressure ionization chambers are usually preferred over scintillators and semiconductor detectors due to their insensitivity to γ-rays. Our findings supported the concept in turn that TCH films also possess similar insensitivity to γ-rays, while

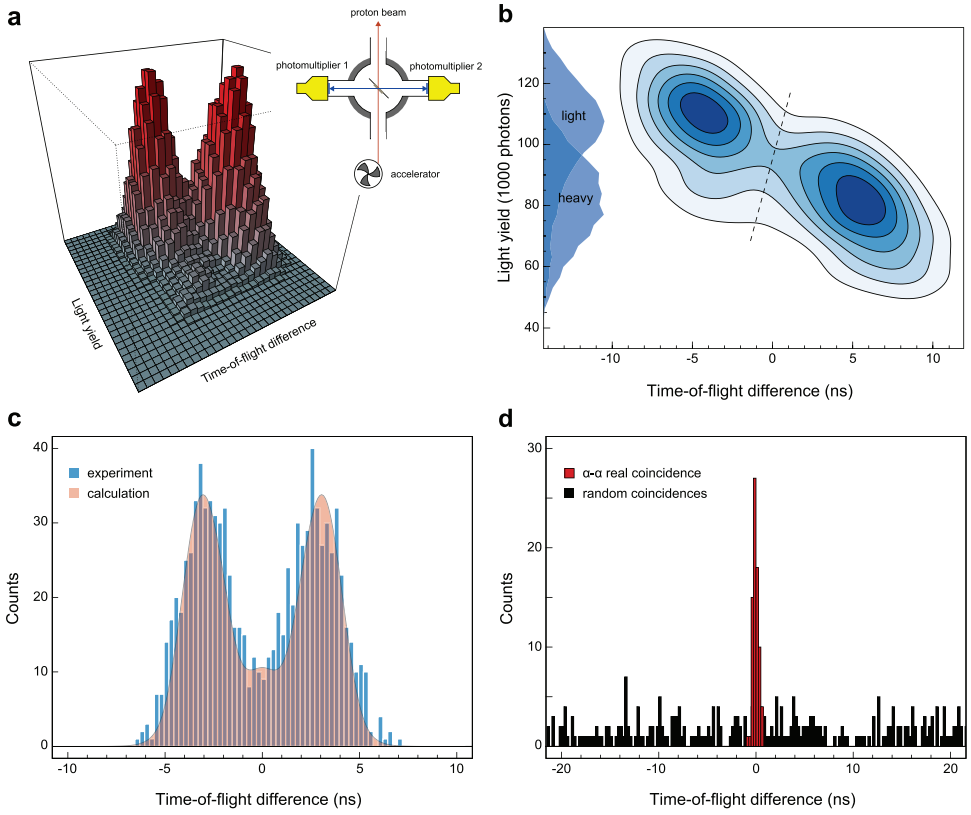

Figure 4. a) Correlation plot of time-of-flight difference between the two fission fragments from $^{235}U(p,ff)$ reaction and their RL yield measured by one of the detector arms. The insert shows the double-arm setup of time-coincidence measurements built for detecting fission fragments with two $Cs_3Cu_2I_5$/PMT or $Cs_3Cu_2I_5$/SiPM detectors; b) Contour plot of the same observables shown in panel (b). The RL yield distribution is separable to contribution of the light and heavy fission fragments by applying the graphical cut (dashed line). c) Distribution of time-of-flight difference between fission fragments from $^{235}U(p,ff)$ reaction, and its fit with GEF model calculation. d) Distribution of time-of-flight difference between α-particles from $^{7}Li(p,\alpha\alpha)$ reaction.

offer a desired simplicity and robustness of operation, as well as enable spectroscopic measurement as demonstrated.

For demonstrating the timing precision and spectroscopic properties of TCH films in nuclear processes, the fission of $^{8}Be^{*}$ synchronously emitting monoenergetic α-particles was proposed using the $^{7}Li(p,\alpha\alpha)$ reaction. As shown in Figure 4d the measured distribution of TOF-difference could be decomposed to events of real ($\alpha\alpha$) and random coincidences (αp, pp) by evaluating the spectroscopic observables. The standard deviation of the $\alpha\alpha$-peak was ≈350 ps, which is a net accuracy of several factors, including contributions from the photon counting statistics, the transit time spread of SiPM detectors, to a lesser extent geometric factors, energy loss straggling, and velocity difference due to the two prefission states in ^{8}Be (16.63 and 16.92 MeV). This finding is in agreement with the analysis of single waveforms in Figure 3a, disclosing the dominating role of light yield in timing precision, while the effect of instrumental and other physical conditions encountered in our test experiments is secondary or even negligible.

3. Conclusion

Overall, polycrystalline TCH-based thin layers prepared with a well-controllable spray-coating method are demonstrated as attractive alternatives of radiation detectors by both overcoming technical obstacles in device fabrication and stability concerns, as well as positioning a new particle scintillator in the middle ground of high-luminosity inorganic single crystals and fast plastic scintillators. Thin-film scintillators of the presented compositions are anticipated as an adequate tool for the high-sensitivity detection of a variety of particle radiations, as they possess most prerequisites that conventional scintillator materials barely satisfy. The effects of long-term storage, exposure to extreme radiation dose, and temperature changes on the luminescence characteristics of the polycrystalline TCH films have been investigated revealing an outstanding functional stability (Figures S14–S16, Supporting Information).

The TCH thin films of appropriate design and combination with photodetectors may offer a competitive or even superior solution in recommended application fields of nuclear safety, space research, or plasma diagnostics in fusion reactors.

4. Experimental Section

Materials: Cesium(I) iodide (CsI, Alfa Aesar, 99.9% trace metals basis), Copper(I) iodide (CuI, Alfa Aesar, Puratronic, 99.998% trace metals basis), acetonitrile (ACN, VWR, 100%), and deionized (DI) water, were used for the preparation of the precursor solutions without further purification. The FTO (fluoride doped tin oxide, Sigma-Aldrich, ≈7 Ω cm^{-2})

covered glass substrates were cleaned with acetone (VWR, 100%), 2-propanol (VWR, 100%), and deionized (DI) water.

Preparation of the Scintillator Layers: The substrates (FTO coated glass or glass) were sonicated for 5 min in acetone, 2-propanol, and DI water before use. Immediately before spray coating the substrates were subjected to 10 min of oxygen plasma treatment as well. In the case of $CsCu_2I_3$, the spray coating solution was prepared by dissolving 0.03 M CsI and 0.06 M CuI in dry acetonitrile, with the addition of 4.5 M H_2O. This transparent solution was spray-coated on the preheated substrates at 60 °C. In the case of $Cs_3Cu_2I_5$, the spray coating solution consisted of 0.052 M CsI and 0.035 M CuI in dry acetonitrile with the addition of 3.4 M H_2O. This transparent solution was spray-coated on the preheated substrates at 70 °C. In the case of both materials the mass loading of the substrates was measured (Figure S1, Supporting Information), and the nominal thickness of the samples was estimated using the density of the different compounds.

Materials Characterization: UV–vis spectra of the layers in both transmission and diffuse reflection mode were recorded with a Shimadzu UV-3600 Plus instrument. Steady-state and time-resolved photoluminescence spectra of the layers was recorded with a FluoroMax spectrofluorimeter equipped DeltaHub TCSPC controller and a NanoLED-295 light source (λ_{max} = 300 nm). The absolute internal quantum yield (QY) of the samples was determined by a JASCO FP-8500 spectrofluorometer equipped with an ILF-835 100 mm integrating sphere. The calibration of the integrating sphere was performed using an ESC-142 calibrated white light source. An excitation wavelength of 300 nm was used in all cases with a 10 nm excitation and emission slit. To control the intensity during the measurements a 1 mm aperture was used as well. More details on the QY determination procedure can be found in the Supporting Information. Top-down and cross section scanning electron microscopy (SEM) images were recorded with a Thermo Scientific Scios 2 SEM-FIB instrument. X-ray diffraction (XRD) measurements were performed with a Brucker D8 Advance instrument with a Cu K_α (λ = 1.5418 Å) X-ray source in the 10–80° 2 theta range with a scan speed of 0.25° min^{-1}. The 3D representation of the crystal structures was generated by the VESTA software package.[43] The reference XRD patterns were simulated by GSAS-II software package.[44] X-ray photoelectron spectroscopy (XPS) measurements were performed with a SPECS instrument equipped with a PHOIBOS 150 MCD 9 hemispherical analyzer. The analyzer was in FAT mode with 40 eV pass energy for acquiring survey scans and 20 eV for high resolution scans. The Al K_α radiation (h_ν = 1486.6 eV) of a dual anode X-ray gun was used as an excitation source and operated at 150 W power. Ten scans were averaged to get a single high-resolution spectrum. The adventitious carbon peak was set at 284.8 eV in all cases. For spectrum evaluation, CasaXPS commercial software package was used.[45] Profilometry measurements were performed with a Veeco Dektak 8 contact-based profilometer equipped with a stylus having a radius of 2.5 µm, and applying a stylus pressure of 30 µN.

Charged-Particle Detection: The measurement setup for the determination of RL yield of TCH scintillators comprised a photomultiplier tube (PMT) of types Photonis XP2262 and ET Enterprises 9813B models, a light integrating hemisphere (38 mm in diameter) with a white reflector surface (EJ-510, Eljen Technology), and a radiation source at a variable distance from the scintillator (Figure S11a, Supporting Information). In α-RL measurements an Am-241 source (2 kBq), in proton-RL measurements a Tandetron linear accelerator was used as radiation source. The setup was placed in a vacuum chamber with controllable air pressure. The energy of α-particles was tuned either by pressure regulation or by distance selection at atmospheric pressure. Under low-pressure conditions the PMT and the scintillator layer were separated with a 4 mm thick PMMA vacuum window. The geometric and transport efficiency of light collection was determined with GEANT4 simulations. The operating voltage of PMTs was set in the range of −1600 to −2000 V, corresponding to a gain of 6×10^6 to 2×10^7. The gain was calibrated by the single-photoelectron response of dark current. The photoconversion efficiency of the PMT cathode was calculated from the specifications of the manufacturer and the measured PL spectra of $Cs_3Cu_2I_5$ and $CsCu_2I_3$ films, which resulted in 22% and 9.5%, respectively. In the fission experiments solid state (silicon) photomultipliers (SiPM) of type ONSEMI ArrayJ-60035 were also used, which have a transit time spread <100 ps in contrast to the 500 ps of the PMT (XP2262). The operating voltage of SiPMs was 29 V. The output signals of the PMT or SiPM were recorded with digital pulse-waveform analyzers CAEN V1730 (500 MS s^{-1}, 14 bit per 2 V, 16 channels) and V1761 (4 GS s^{-1}, 10 bit per 1 V, 2 channels).

Compton-Coincidence Setup: The CCT setup was based on a method utilizing the production of electrons in the scintillator material and the measurement of its light response in time coincidence mode[41]. The CCT setup (Figure S11b, Supporting Information) was planned to overcome two essential obstacles one encounters in the single-electron measurement of thin layer samples. One was the geometry factor of reduced specular volume viewed by the γ-detector (HPGe), which in combination with the orders of magnitude lower γ-absorption probability requires a high-activity γ-source (Cs-137, 2.1 GBq). The second obstacle was the escape of Compton electrons from the thin layer, which becomes critical with increasing energy above 100 keV for a layer thickness of 100 µm. The Compton electrons had a well-defined angle with respect to the beam axis and the angle of the γ-detector, around which the angle of the scintillator layer can be fine-tuned to minimize the ratio of lost events.

Fission-Coincidence Setup: The actinide fission measurement was performed at the MGC-20 cyclotron of ATOMKI using a 12 MeV proton beam at 10 nA beam current and 10% filling factor. The beam bombarded a 30 µg cm^{-2} thick ^{235}U target on carbon backing, which was tilted by 45° with respect to the beam axis facing two $Cs_3Cu_2I_5$ (50 µm)/PMT detectors each placed at a distance of 95 mm from the target (Figure 4a).

The ^8Be fission measurement was performed at the Tandetron accelerator of ATOMKI using a 1.87 MeV continuous proton beam at 15 nA. The beam bombarded a 500 nm thick LiF film on a 1.5 µm Al foil (99%, Goodfellow), which was tilted by 45° with respect to the beam axis facing two $Cs_3Cu_2I_5$ (50 µm)/SiPM detectors each placed at 40 mm from the target. The principal arrangement of the setup is the same as shown in Figure 4a. The ^8Be prefission nuclei were excited by proton capture on ^7Li (Q = 17.255 MeV) populating the 18.91 MeV state (Γ = 122 keV), which directly decays to the 16.92 and 16.63 MeV states by γ-emission. These states split up to two monoenergetic (≈8.5 MeV) α-particles emitted at a velocity of 2.02 cm ns^{-1}.

Statistical Analysis: The mean value of the radioluminescence light yield distributions was constructed of an ensemble average from repeated measurements on five different samples using two different types of PMT detectors. For each setting the single-electron response (Figure S17a, Supporting Information) was analyzed to obtain the PMT gain. Stochastic processes such as electronic noise, cathode efficiency, and radial sensitivity variations of the PMT were relatively low, therefore a net uncertainty of the light yield measurement was deduced as ≈8%.

The width of the light yield distributions, which was a direct measure of energy resolving power at a given particle energy, was predominantly of statistical nature, corresponding to a minimum FWHM value 7%, while systematic variations had a minor contribution ≈2%, which could be attributed to layer inhomogeneity, small deviations in the light collection setup, as well as uncertainties in the cathode quantum efficiency deduced by the spectral matching between the PMT sensitivity and PL emission of the TCH layers (Figure S17b, Supporting Information). The observed widths were composed of minor contributions of the photon counting statistics (<4%), and of major contributions of gain variation of the PMT detectors (≈7%).

The decay components of the mean waveforms were fitted with a nonlinear regression model using a biexponential function with 4 parameters (2 amplitudes, 2 exponents). The statistical analysis used the R code nls.LM() based on the Levenberg-Marquardt algorithm. The net variations were determined by combining the statistical parameters over the various measurement settings for a series of samples and PMT detectors, similarly to the procedure of the light yield analysis.

The statistical parameters of light yield distributions were also determined with the same nonlinear regression model using Gaussian distributions. Uncertainties given for quantities were purely statistical including variance of fitting procedures and ensemble analysis, while systematic error was not involved.

Supporting Information

Supporting Information is available from the Wiley Online Library or from the author.

Acknowledgements

The authors thank Zs. Fülöp for his continuous support and fruitful orientating discussions throughout the project. The authors also thank J. Kopniczky and B. Hopp for their help in the profilometry measurements, O. Dömötör and E.A. Enyedy for the use and assistance in the steady state PL and PL lifetime measurements, D. Ungor and E. Csapó for the use and their assistance in the PLQY measurements, as well as J. Molnár for providing scintillator samples for the reference measurements. This work was supported by the projects TKP2021-NKTA-42 and TKP-2021-NVA-19 financed by the National Research, Development and Innovation Fund of the Ministry for Innovation and Technology, Hungary. The research was further supported by the National Research, Development and Innovation Office (NKFIH) through the FK-138888 project. G.F.S also acknowledge the financial support of the János Bolyai Research Scholarship of the Hungarian Academy of Sciences.

Conflict of Interest

A Hungarian patent application and a PCT patent application (PCT/HU2022/050066) have been filed by certain authors of this paper and their institutions.

Data Availability Statement

The data that support the findings of this study are available from the corresponding author upon reasonable request.

Keywords

alpha-particle detections, cesium-copper-halides, detectors, ionizing radiations, perovskites, polycrystalline, scintillators

Received: June 10, 2022
Revised: August 5, 2022
Published online: September 18, 2022

[1] C. Dujardin, E. Auffray, E. Bourret-Courchesne, P. Dorenbos, P. Lecoq, M. Nikl, A. N. Vasil'ev, A. Yoshikawa, R.-Y. Zhu, *IEEE Trans. Nucl. Sci.* **2018**, *65*, 1977.
[2] Y. He, I. Hadar, M. G. Kanatzidis, *Nat. Photonics* **2022**, *16*, 14.
[3] H. Wei, J. Huang, *Nat. Commun.* **2019**, *10*, 1066.
[4] W. Li, L. Liu, M. Tan, Y. He, Ch. Guo, H. Zhang, H. Wei, B. Yang, *Adv. Funct. Mater.* **2021**, *31*, 2107843.
[5] Q. Chen, J. Wu, X. Ou, B. Huang, J. Almutlaq, A. A. Zhumekenov, X. Guan, S. Han, L. Liang, Z. Yi, J. Li, X. Xie, Y. Wang, Y. Li, D. Fan, D. B. L. Teh, A. H. All, O. F. Mohammed, O. M. Bakr, T. Wu, M. Bettinelli, H. Yang, W. Huang, X. Liu, *Nature* **2018**, *561*, 88.
[6] M. Nikl (Ed.), *Nanocomposite, Ceramic, and Thin Film Scintillators*, Jenny Stanford Publishing, New York, NY **2016**.
[7] J. J. Toledo-Garrido, J. Galdon-Quiroga, E. Viezzer, G. Birkenmeier, V. Olevskaia, M. Balden, J. Garcia-Lopez, M. C. Jimenez-Ramos, M. Rodriguez-Ramos, G. Anda, M. Videla-Trevin, M. Garcia-Munoz, *J. Instrum.* **2022**, *17*, P02026.
[8] G. Rusev, M. Jandel, B. Baramsai, E. M. Bond, T. A. Bredeweg, A. Couture, J. K. Daum, A. Favalli, K. D. Ianakiev, M. L. Iliev, S. Mosby, A. R. Roman, R. K. Springs, J. L. Ullmann, C. L. Walker, in *Proc. SPIE 9593, HardX-Ray, Gamma-Ray, and Neutron Detector Physics XVII* (Eds: L. Franks, R. B. James, M. Fiederle, A. Burger), SPIE, Bellingham, WA **2015**, p. 959314.
[9] E. V. D. van Loef, P. Dorenbos, C. W. E. van Eijk, K. Krämer, H. U. Güdel, *Appl. Phys. Lett.* **2001**, *79*, 1573.
[10] C. Kim, W. Lee, A. Melis, A. Elmughrabi, K. Lee, C. Park, J.-Y. Yeom, *Crystals* **2021**, *11*, 669.
[11] M. Zhuravleva, L. Stand, H. Wei, C. Hobbs, L. A. Boatner, J. O. Ramey, K. Shah, A. Burger, E. Rowe, P. Bhattacharya, E. Tupitsyn, C. L. Melcher, in *Nucl. Sci. Symp. Med. Imaging Conf. (2013 NSS/MIC)*, IEEE, Piscataway, NJ **2013**, https://doi.org/10.1109/NSSMIC.2013.6829669.
[12] H. Y. Jeong, J. H. Lee, S. Y. Lee, J. Lee, S. O. Cho, *ACS Omega* **2021**, *6*, 33224.
[13] V. V. Nagarkar, S. R. Miller, V. Gelfandbein, U. Shirwadkar, V. Gaysinskiy, *Nucl. Instruments Methods Phys. Res. Sect. A Accel. Spectrometers, Detect. Assoc. Equip.* **2011**, *652*, 271.
[14] Y. Zhu, S. Qian, Z. Wang, H. Guo, L. Ma, Z. Wang, Q. Wu, *Opt. Mater. (Amst).* **2020**, *105*, 109964.
[15] Q. He, C. Zhou, L. Xu, S. Lee, X. Lin, J. Neu, M. Worku, M. Chaaban, B. Ma, *ACS Mater. Lett.* **2020**, *2*, 633.
[16] Z. Guo, J. Li, R. Pan, J. Cheng, R. Chen, T. He, *Nanoscale* **2020**, *12*, 15560.
[17] M. Li, Z. Xia, *Chem. Soc. Rev.* **2021**, *50*, 2626.
[18] R. Roccanova, A. Yangui, H. Nhalil, H. Shi, M.-H. Du, B. Saparov, *ACS Appl. Electron. Mater.* **2019**, *1*, 269.
[19] Y. Li, P. Vashishtha, Z. Zhou, Z. Li, S. B. Shivarudraiah, C. Ma, J. Liu, K. S. Wong, H. Su, J. E. Halpert, *Chem. Mater.* **2020**, *32*, 5515.
[20] L. Xie, B. Chen, F. Zhang, Z. Zhao, X. Wang, L. Shi, Y. Liu, L. Huang, R. Liu, B. Zou, Y. Wang, *Photonics Res* **2020**, *8*, 768.
[21] M. Zhang, J. Zhu, B. Yang, G. Niu, H. Wu, X. Zhao, L. Yin, T. Jin, X. Liang, J. Tang, *Nano Lett.* **2021**, *21*, 1392.
[22] L. Lian, M. Zheng, W. Zhang, L. Yin, X. Du, P. Zhang, X. Zhang, J. Gao, D. Zhang, L. Gao, G. Niu, H. Song, R. Chen, X. Lan, J. Tang, J. Zhang, *Adv. Sci.* **2020**, *7*, 2000195.
[23] T. Yanagida, *Proc. Japan Acad. Ser. B* **2018**, *94*, 75.
[24] S. Cheng, A. Beitlerova, R. Kucerkova, M. Nikl, G. Ren, Y. Wu, *Phys. Status Solidi – Rapid Res. Lett.* **2020**, *14*, 2000374.
[25] X. Li, J. Chen, D. Yang, X. Chen, D. Geng, L. Jiang, Y. Wu, C. Meng, H. Zeng, *Nat. Commun.* **2021**, *12*, 3879.
[26] J. Zhou, K. An, P. He, J. Yang, C. Zhou, Y. Luo, W. Kang, W. Hu, P. Feng, M. Zhou, X. Tang, *Adv. Opt. Mater.* **2021**, *9*, 2002144.
[27] S. Cheng, M. Nikl, A. Beitlerova, R. Kucerkova, X. Du, G. Niu, Y. Jia, J. Tang, G. Ren, Y. Wu, *Adv. Opt. Mater.* **2021**, *9*, 2100460.
[28] X. Ouyang, R. Lin, Y. Ding, Y. Liang, W. Zheng, L. Chen, X. Song, F. Huang, X. Ouyang, *Mater. Chem. Front.* **2021**, *5*, 4739.
[29] R. Lin, Y. Ding, W. Zheng, M. Jin, L. Chen, X. Ouyang, F. Huang, *Cell Reports Phys. Sci.* **2021**, *2*, 100437.
[30] S. Fang, Y. Wang, H. Li, F. Fang, K. Jiang, Z. Liu, H. Li, Y. Shi, *J. Mater. Chem. C* **2020**, *8*, 4895.
[31] S. Cheng, A. Beitlerova, R. Kucerkova, E. Mihokova, M. Nikl, Z. Zhou, G. Ren, Y. Wu, *ACS Appl. Mater. Interfaces* **2021**, *13*, 12198.
[32] D. Yuan, *ACS Appl. Mater. Interfaces* **2020**, *12*, 38333.
[33] Y. Zhou, X. Wang, T. He, H. Yang, C. Yang, B. Shao, L. Gutiérrez-Arzaluz, O. M. Bakr, Y. Zhang, O. F. Mohammed, *ACS Energy Lett.* **2022**, *7*, 844.

[34] N. Li, Z. Xu, Y. Xiao, Y. Liu, Z. Yang, S. (Frank) Liu, *Adv. Opt. Mater.* **2022**, *10*, 2102232.
[35] Z. Guo, J. Li, Y. Gao, J. Cheng, W. Zhang, R. Pan, R. Chen, T. He, *J. Mater. Chem. C* **2020**, *8*, 16923.
[36] X. Mo, T. Li, F. Huang, Z. Li, Y. Zhou, T. Lin, Y. Ouyang, X. Tao, C. Pan, *Nano Energy* **2021**, *81*, 105570.
[37] T. Ihara, *Phys. Rev. B* **2016**, *93*, 235442.
[38] I. V. Khodyuk, P. Dorenbos, *IEEE Trans. Nucl. Sci.* **2012**, *59*, 3320.
[39] H. Alva-Sánchez, A. Zepeda-Barrios, V. D. Díaz-Martínez, T. Murrieta-Rodríguez, A. Martínez-Dávalos, M. Rodríguez-Villafuerte, *Sci. Rep.* **2018**, *8*, 17310.
[40] V. I. Tretyak, *Astropart. Phys.* **2010**, *33*, 40.
[41] J. D. Valentine, B. D. Rooney, *Nucl. Instruments Methods Phys. Res. Sect. A Accel. Spectrometers, Detect. Assoc. Equip.* **1994**, *353*, 37.
[42] K.-H. Schmidt, B. Jurado, C. Amouroux, C. Schmitt, *Nucl. Data Sheets* **2016**, *131*, 107.
[43] K. Momma, F. Izumi, *J. Appl. Crystallogr.* **2011**, *44*, 1272.
[44] B. H. Toby, R. B. Von Dreele, *J. Appl. Crystallogr.* **2013**, *46*, 544.
[45] N. Fairley, V. Fernandez, M. Richard-Plouet, C. Guillot-Deudon, J. Walton, E. Smith, D. Flahaut, M. Greiner, M. Biesinger, S. Tougaard, D. Morgan, J. Baltrusaitis, *Appl. Surf. Sci. Adv.* **2021**, *5*, 100112.